TEL AVIV UNIVERSITY

The Iby and Aladar Fleischman Faculty of Engineering
The Zandman-Slaner School of Graduate Studies

ONCOMETABOLITE FINGERPRINTING USING FLUORESCENT SINGLE-WALLED CARBON NANOTUBES

A thesis submitted toward the degree of
Master of Science in Biomedical Engineering

By

Dean Amir

October 2021

TEL AVIV UNIVERSITY

The Iby and Aladar Fleischman Faculty of Engineering
The Zandman-Slaner School of Graduate Studies

ONCOMETABOLITE FINGERPRINTING USING FLUORESCENT SINGLE-WALLED CARBON NANOTUBES

A thesis submitted toward the degree of
Master of Science in Biomedical Engineering

By

Dean Amir

This research was carried out in The Department of Biomedical Engineering
Under the supervision of Dr. Gili Bisker

October 2021

Acknowledgements

Abstract

The production of oncometabolites is the direct result of mutagenesis in key cellular metabolic enzymes, appearing typically in cancers such as glioma, leukemia, and glioblastoma. Once accumulated, oncometabolites promote cancerous transformations by interfering with important cellular functions. Hence, the ability to sense and quantify oncometabolites is essential for cancer research and clinical diagnosis. In this work, we present a near-infrared optical nanosensor for a known oncometabolite, D-2-hydroxyglutarate (D2HG), discovered in a screening of a library of fluorescent single-walled carbon nanotubes (SWCNTs) functionalized with single-stranded DNA. The high-throughput screening procedure was enabled owing to a dedicated software for controlling the spectrometry devices and spectra acquisition developed for this purpose. The screening revealed (ATTT)$_7$-SWCNT as a sensor for D2HG, exhibiting a fluorescence intensity increase upon the interaction with D2HG. The fluorescence response of the sensor does not appear to be attributed to basic chemical features of the target analytes tested, and is shown to discriminate D2HG from other related metabolites, including its enantiomer L-2-hydroxyglutarate. Further, the fluorescence modulation is dependent on the analyte concentration and the SWCNT chirality, showing up to 40.7% and 28.2% increase of the (6,5)-chirality peak and the (9,5)- and (8,7)-chirality joint peak, at 572 nm and 730 nm excitation, respectively, in the presence of 10 mM D2HG. The work opens new opportunities for molecular recognition of oncometabolites which can advance basic cancer metabolism research.

Publications

- Dean Amir, Adi Hendler-Neumark, Verena Wulf, Roni Ehrlich, and Gili Bisker, "Oncometabolite fingerprinting using fluorescent single-walled carbon nanotubes", *Advanced Materials Interfaces,* 2021.

Abstract: The production of oncometabolites is the direct result of mutagenesis in key cellular metabolic enzymes, appearing typically in cancers such as glioma, leukemia, and glioblastoma. Once accumulated, oncometabolites promote cancerous transformations by interfering with important cellular functions. Hence, the ability to sense and quantify oncometabolites is essential for cancer research and clinical diagnosis. In this work, we present a near-infrared optical nanosensor for a known oncometabolite, D-2-hydroxyglutarate (D2HG), discovered in a screening of a library of fluorescent single-walled carbon nanotubes (SWCNTs) functionalized with single-stranded DNA. The screening revealed $(ATTT)_7$-SWCNT as a sensor for D2HG, exhibiting a fluorescence intensity increase upon the interaction with D2HG. The fluorescence response of the sensor does not appear to be attributed to basic chemical features of the target analytes tested, and is shown to discriminate D2HG from other related metabolites, including its enantiomer L-2-hydroxyglutarate. Further, the fluorescence modulation is dependent on the analyte concentration and the SWCNT chirality, showing up to 40.7% and 28.2% increase of the (6,5)-chirality peak and the (9,5)- and (8,7)-chirality joint peak, at 572 nm and 730 nm excitation, respectively, in the presence of 10 mM D2HG. Our work opens new opportunities for molecular recognition of oncometabolites which can advance basic cancer metabolism research.

- Roni Ehrlich, Adi Hendler-Neumark, Verena Wulf, Dean Amir, and Gili Bisker, "Optical Nanosensors for Real-Time feedback on Insulin Secretion by β-cells", *Small*, July 2021.

Abstract: Quantification of insulin is essential for diabetes research in general, and for the study of pancreatic β-cell function in particular. Herein, fluorescent single-walled carbon nanotubes (SWCNT) are used for the recognition and real-time quantification of insulin. Two approaches for rendering the SWCNT sensors for insulin are compared, using surface functionalization with either a natural insulin aptamer with known affinity to insulin, or a synthetic lipid-poly(ethylene glycol) (PEG) (C_{16}-PEG(2000Da)-Ceramide), both of which show a modulation of the emitted fluorescence in response to insulin. Although the PEGylated-lipid has no prior affinity to insulin, the response of C_{16}-PEG(2000Da)-Ceramide-SWCNTs to insulin is more stable and reproducible compared to the insulin aptamer-SWCNTs. The SWCNT sensors successfully detect insulin secreted by β-cells within the complex environment of the conditioned media. The insulin is quantified by comparing the SWCNTs fluorescence response to a standard calibration curve, and the results are found to be in agreement with an enzyme-linked immunosorbent assay. This novel analytical tool for real time quantification of insulin secreted by β-cells provides new opportunities for rapid assessment of β-cell function, with the ability to push forward many aspects of diabetes research.

Contents

List of figures

1.1. Introduction

1.1.1 Oncometabolites

Mutations in enzymatic components of cellular metabolic pathways are typical of many types of cancer[1–9]. These mutations can be of a loss-of-function type, leading to the accumulation of the enzyme's substrate metabolites, or of a gain-of-function type, leading to the production of a different product[1,2,4–7,9]. Either way, the energy production process is severely damaged. These local changes in the levels of involved metabolites or products can indicate an ongoing process of a cancerous transformation, and even further contribute to its escalation, rendering them *oncometabolites*[1–9].

D-2-hydroxyglutarate (D2HG) is a product of the gain-of-function-mutated enzymes isocitrate dehydrogenase (IDH1/IDH2), whereas the normal mitochondrial form plays a role in the tricarboxylic acid (TCA) cycle by producing α-ketoglutarate[1,2,4–9]. Hence, an accumulation of D2HG in the mitochondria indicates a mutagenesis of IDH and interruption of the TCA cycle, implying that the cell is in a state of pseudo-hypoxia (resembling a state of low oxygen levels), and mainly relying on glycolysis for energy production (**Scheme 1.1**)[4].
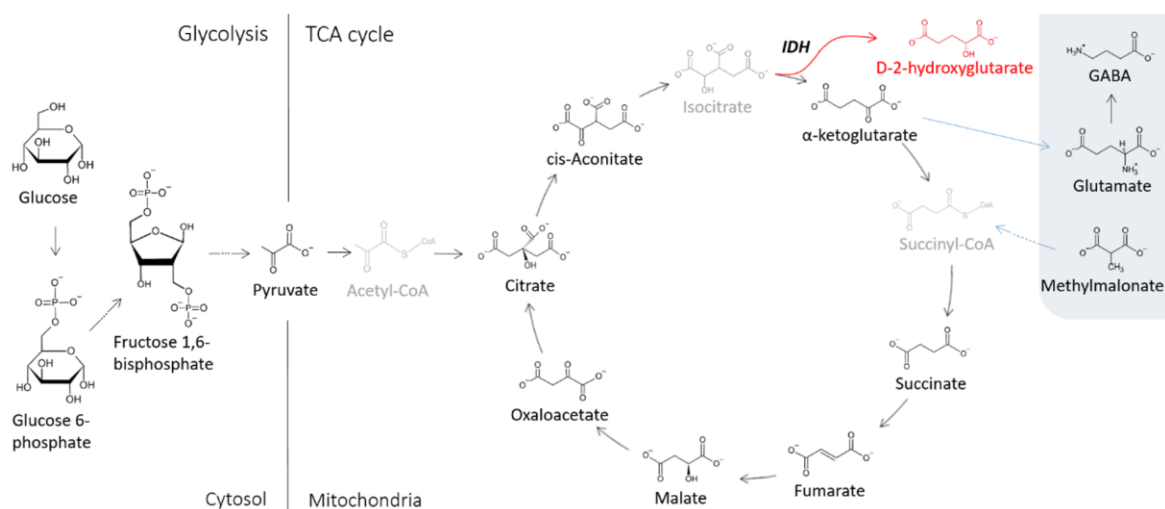
Scheme 1.1. Overview of glycolysis and the TCA cycle, with additional adjacent pathways. The red arrow represents the mutant form of isocitrate dehydrogenase (IDH), which produces D2HG. Molecular structures of the metabolites shown in black are screened in this study.

Normally, as a minor metabolic byproduct, D2HG levels are kept low as *D*-2-hydroxyglutarate dehydrogenase (D2HGDH) converts it to α-ketoglutarate[1,10]. However, D2HGDH does not prevent D2HG accumulation in the case of overproduction[10]. Moreover, a congenital loss of D2HGDH causes D2HG accumulation, which can lead to a severe brain damage in a rare condition called *D*-2-hydroxyglutarate aciduria[1,10].

The accumulation of D2HG was shown to inhibit a group of enzymes named a-ketoglutarate-dependent dioxygenases (aKGdd), resulting in the promotion of mutagenesis by epigenetic modification of DNA and histone hypermethylation[1,4,5,7]. Notably, IDH1-mutated tumors were shown to exhibit DNA hypermethylation in gliomas and leukemia, and also histone hypermethylation[1,5–7,9,11]. Accumulation of 2-hydroxyglutarate (both D and L optical isomers) was found to suppress cell-proliferation regulation[1,9]. As a demonstration of D2HG cellular potency, it was shown that incubating hematopoietic stem cells with D2HG alters differentiation patterns and promotes immune resistance[1,6].

IDH mutations and D2HG accumulation were found in gliomas and glioblastomas, and D2HG accumulation is suspected to be sufficient for promoting the development of acute myeloid leukemia (AML)[1,6]. Another possible oncogenic mechanism linked to D2HG abundance, is its ability to shift cellular redox equilibrium towards overproduction of reactive oxygen species (ROS), which are well-known oncogenic agents[4]. The same mechanism was also found to impair immune antitumor activity[1,8].

The ability to sense and measure D2HG in various contexts is highly important for cancer research and possibly for medical diagnosis. Existing quantification methods include standard analytical techniques such as calorimetry or gas chromatography-mass spectrometry. However, they are costly, time consuming, and cannot provide real-time information. In contrast, functionalized single-walled carbon nanotubes (SWCNTs) can be

used as optical nanosensors for the recognition and quantification of small molecules, with real-time feedback[12–16].

1.1.2 Single-walled Carbon Nanotubes

Single-walled carbon nanotubes can be described as single-atom-thick graphene sheets rolled up to cylinders, with diameters ranging from 0.7 to 3 nm[17]. As rolling up a hexagonal lattice, such as graphene, can be done in multiple directions, SWCNTs can vary in their structure, resulting in different chiralities[18,19]. Chiral SWCNTs are denoted by two positive integers n and m as (n,m)-SWCNT **(Figure 1.1)** and they exhibit different physical, chemical, electronic, and optical properties, such as different fluorescence excitation and emission peaks **(Figure 1.2)**[20,21]. Due to the electronic band-gap between valence and conduction band, semiconducting SWCNT fluoresce in the near-infrared (nIR) range, where absorption, scattering, and autofluorescence of biological tissues are reduced, rendering SWCNTs favorable for biomedical sensing and imaging applications[22–36].

Being hydrophobic, SWCNTs can be suspended using non-covalent surface functionalization via hydrophobic interactions with amphiphilic molecules (polymer-lipid composites, surfactants), or via π-π stacking interactions, e.g. with single-stranded DNA[37–39]. SWCNTs can only emit fluorescence when functionalized and suspended.
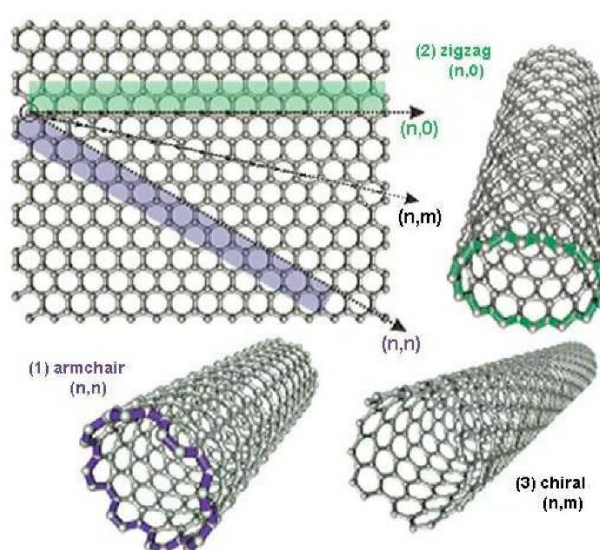
Figure 1.1. Chirality in single-walled carbon nanotubes. n and m denote the 'roll-up' vector of a graphene sheet. Source: Scholarly Community Encyclopedia
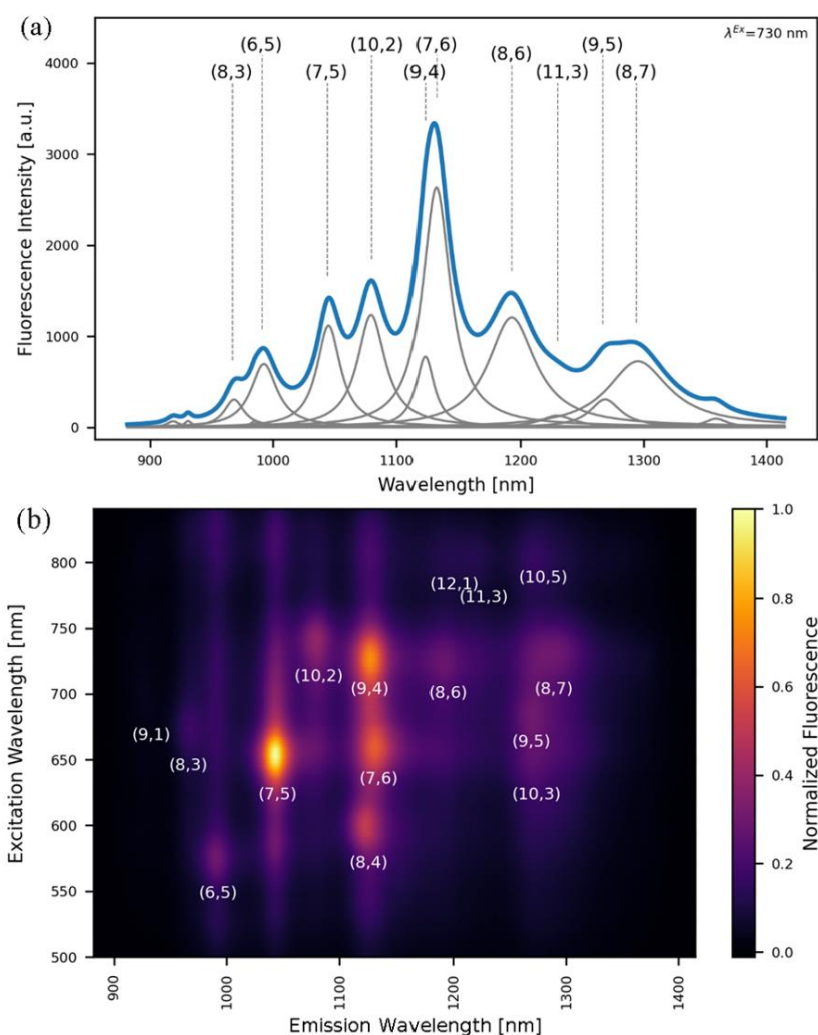
Figure 1.2. The contribution of SWCNTs of multiple chiralities to the total near-IR fluorescence emission of a ssDNA-SWCNT suspension, upon laser excitation of (a) a wavelength of 730 nm, (b) 500-800 nm wavelength range.

The combination of SWCNT and its surface functionalization forms unique three-dimensional spatial and chemical structures, capable of providing rather specific binding sites for molecular recognition, indicated through measurable alterations in the SWCNT fluorescence profile[40–43].

This approach has been demonstrated to detect small molecules[25,44–46] such as hormones[26], volatiles[47,48], microRNAs[49], and neurotransmitters[50–52], and larger molecules, such as proteins[53–58] and enzymes[59–61]. Owing to their ease-of-use and nIR fluorescence, utilization of functionalized SWCNTs allows for optical signal transduction in real-time in response to analytes of interests. The functionalized SWCNTs sensors can often be used to both detect and quantify a target analyte, using fluorescence modulation measurements (**Figure 1.3**).
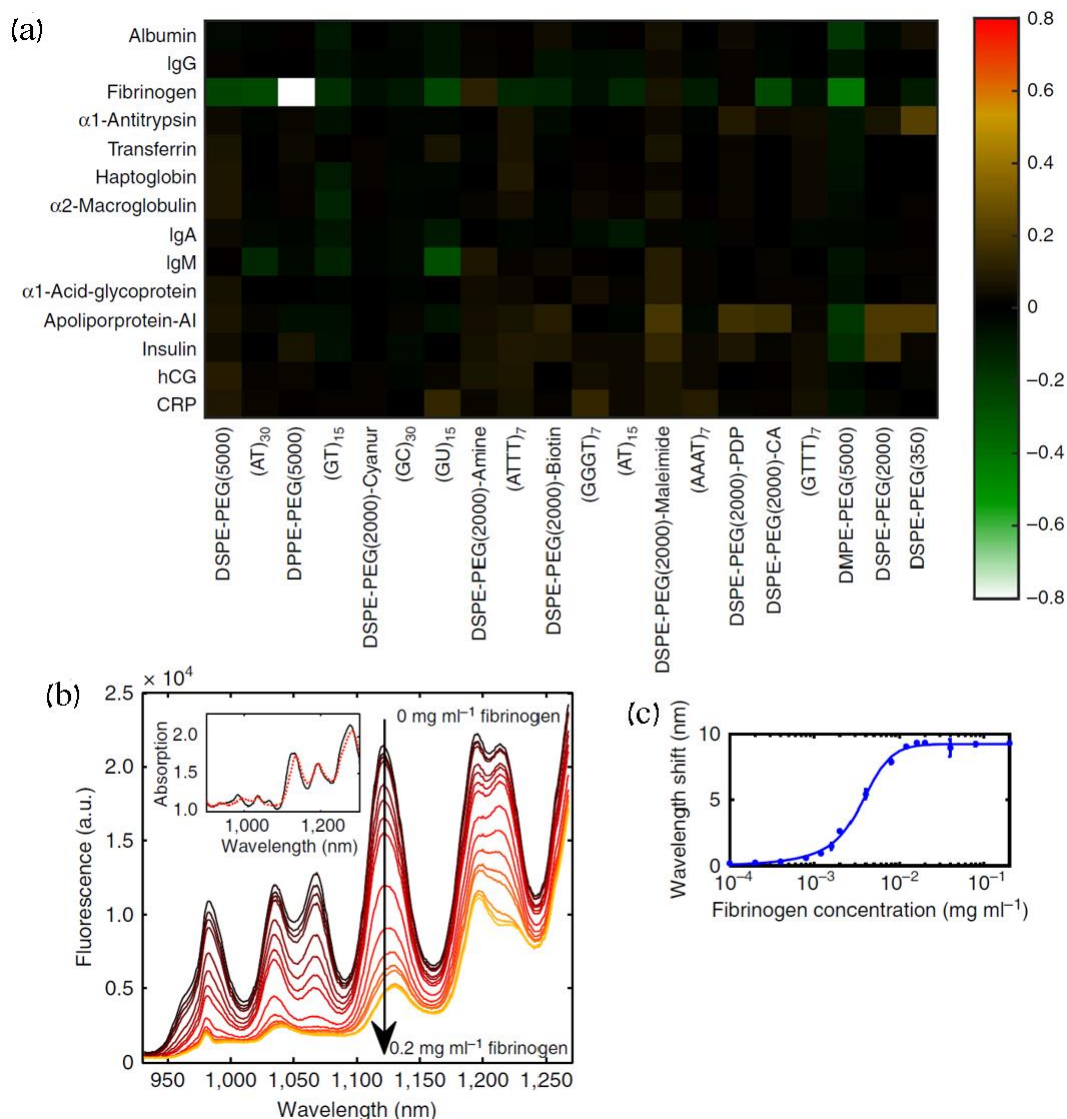
Figure 1.3. Functionalized SWCNTs as sensors. This example describes a process of characterizing a SWCNT-based sensor for the coagulation protein Fibrinogen. **(a)** The screening process, with a library of blood components on the vertical axis, and a library of functionalization agents on the horizontal axis. **(b)** Modulation of fluorescence intensity in response to different concentrations of the analyte. **(c)** Shifts of the peak wavelength of a certain SWCNT chirality in response to different analyte concentrations, and a calibration curve fitting the data, which can be utilized to quantify the analyte. Adopted from Bisker et at. 2015[53].

Recently, our group developed a sensor for the detection and quantification of the peptide hormone insulin, based on SWCNTs functionalized with synthetic PEGylated lipids. Quantification results were in agreement with traditional methods, and the sensor was successfully used to detect insulin secreted by pancreatic β-cells[55] (**Figure 1.4**).
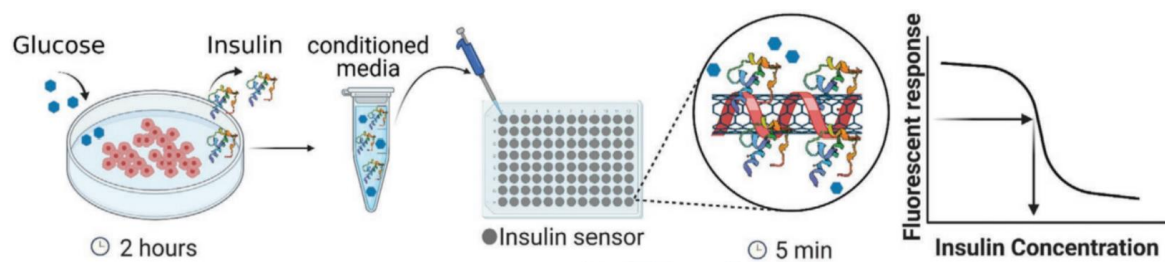
Figure 1.4. An example of a fluorescent SWCNT-based sensor developed by our group. This sensor successfully detects and quantifies insulin secreted from pancreatic β-cells (Adopted from Ehrlich et at.[55])

1.2. Research goal

Here, we present a ssDNA-SWCNT sensor for the detection and quantification of the oncometabolite D2HG. After screening a library of 9 ssDNA-functionalized SWCNT samples with a library of cellular metabolite targets, we identified (ATTT)$_7$-SWCNT as an optical sensor for D2HG. The optical response cannot be attributed to non-selective molecular features such as the number of carbon atoms, charge, or molecular weight. Further, the fluorescence response is shown to be excitation-wavelength dependent, through the excitation of SWCNT of different chiralities, and is capable of distinguishing between the optical isomers of 2-hydroxyglutarate. Our findings can advance the current research and diagnosis toolbox in cancer and cellular metabolism.

1.3. Methods

Materials. Analytes were purchased from Sigma-Aldrich (Fumarate, Succinate, Pyruvate, Glucose 6-phosphate, Glutamate, GABA, Oxaloacetate), Santa Cruz Biotechnology (α-ketoglutarate, cis-aconitate), Bio-Lab (Citrate), Carlo Erga Reagents (Malate), Merck (Glucose), CarboSynth (Fructose 1,6-bisphosphate), Cayman Chemical (Methylmalonate, D-2-hydroxyglutarate). Isocitrate was not included in this study due to the lack of availability of a pure physiological D enantiomer[59]. Acetyl-CoA, succinyl-CoA and other glycolysis components were not included owing to their larger size compared to the rest of the small molecule analytes. HiPCO single-walled carbon nanotubes were purchased from NanoIntegris. DNA oligonucleotides were purchased from Integrated DNA Technologies.

Chemical features data. Net charge and molar mass were calculated using PubChem 2.1, Hydrophobicity was calculated using XLogP3 3.0, and the number of hydrogen-bond donors, hydrogen-bond acceptors and the topological polar surface area were calculated using Cactvs 3.4.8.18. All were extracted from PubChem website (National Institutes of Health)[60].

Analyte preparation. All analyte powders were dissolved in PBS (1x) to a concentration of 10 mM, vortexed thoroughly until no aggregates were visual, then vortexed again, aliquoted, and frozen. New aliquots were unfrozen to complete fluidity and vortexed for each experimental session, and kept in an ice bath throughout the process.

ssDNA-SWCNT Suspension. For a 1 mL aqueous suspension, 2 mg ssDNA were mixed with 1 mg SWCNTs in 0.1M NaCl, vortexed thoroughly and bath-sonicated (80 Hz, 100% Amp for 10 min, Elma P-30H). Subsequently, the solution was tip-sonicated twice in a fresh ice bath (3 mm tip diameter, ~4 W for 20 min, QSonica Q125) and centrifuged twice (16100 rcf for 90 min, Eppendorf) where 80% of the supernatant was collected after each round. The suspension concentrations were calculated using absorption at 632 nm with $\varepsilon_{632nm} = 0.036$ L g^{-1} cm^{-1}, measured by UV−vis−nIR spectroscopy (Shimadzu UV-3600i Plus).

Screening. The ssDNA-SWCNT suspensions were diluted to 1 mg L^{-1} in PBS and 145 μL were added to each necessary well in 96-well plates, such that every ssDNA-SWCNT-analyte combination is repeated 3 times. 5 μL of 10 mM analyte solutions were added to the wells for

16

a total volume of 150 µL, resulting in a final analyte concentration of 0.33 mM. Following 15 minutes incubation, the fluorescence spectra were acquired from each well using a cryogenically-cooled InGaAs detector (PyLoN-IR, Princeton Instruments, Teledyne Technologies), coupled to a spectrometer (SpectraPro® HRS-300, Princeton Instruments, Teledyne Technologies). Fluorescence excitation was achieved using a supercontinuum laser (SuperK EXTREME, NKT Photonics) at 20.5 mW (730 nm).

Limit of detection (LOD) calculation. The minimal detectable concentration is limited by the noise level of the instrumentation, calculated as three times the standard deviation (STD) of the measured fluorescence signal of a buffer solution alone (background noise) divided by the mean, as well as random errors that arise from the handling of samples, including on addition of an analyte to a sensor solution (pipetting, stabilization, etc.), calculated as the normalized STD of readings of the initial SWCNT suspension following the addition of a buffer solution of the same volume as the analytes added. The LOD is taken as the maximal value between the two error calculations.

1.4. Results

1.4.1. Initial characterization of SWCNTs suspensions

HiPCO SWCNTs were suspended with each of the selected sequences of 9 DNA oligonucleotides (**Table 1.1**), using tip-sonication.

Name	Sequence
(GT)$_{15}$-*(I)*	GTG TGT GTG TGT GTG TGT GTG TGT GTG TGT GAT CTA AGG CGT GTA T
(GT)$_{15}$-*(II)*	GTG TGT GTG TGT GTG TGT GTG TGT GTG TGT CTA AGG CGT GTA T
(GT)$_{15}$-*(III)*	GTG TGT GTG TGT GTG TGT GTG TGT GTG TGT GAT GCG TGT CTA AGA T
(ATTT)$_3$	ATT TAT TTA TTT
(ATTT)$_7$	ATT TAT TTA TTT ATT TAT TTA TTT ATT T
(TAT)$_4$	TAT TAT TAT TAT
(GTTT)$_7$	GTT TGT TTG TTT GTT TGT TTG TTT GTT T
(GC)$_{30}$	GCG CGC GCG CGC GCG CGC GCG CGC GCG CGC GCG CGC GCG CGC GCG CGC GCG CGC GCG CGC
T$_{30}$	TTT TTT TTT TTT TTT TTT TTT TTT TTT TTT

Table 1.1. DNA sequences used for suspending SWCNT.

Indicative of successful processing, the suspensions exhibited typical absorption peaks (**Figure 1.5a**), and fluorescence emission in the nIR range with distinguishable peaks of the various chiralities in the mixture (**Figure 1.5 b** and **c**). Differences in the fluorescence emission profiles were noticeable between the different ssDNA-SWCNT suspensions, owing to the distinct interactions between each of the ssDNA and the various SWCNTs chiralities[61]. In particular, some of the DNA sequences are known as resolving sequences used for the separation and purification of selected chiralities[19,65–68].
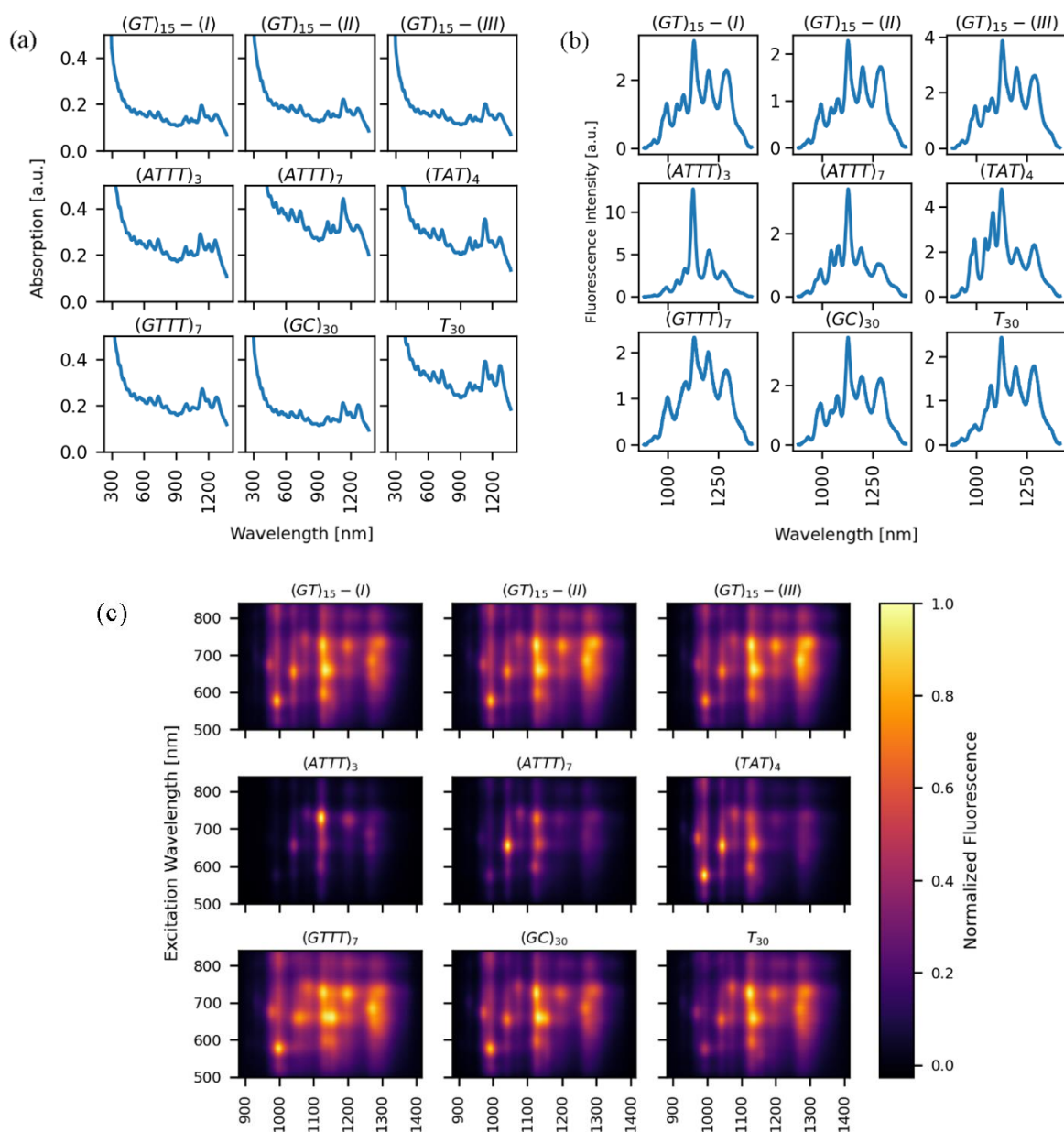
Figure 1.5. Characterization of the ssDNA-SWCNT suspensions used for screening. (a) Absorption spectra. (b) Fluorescence emission. (c) Excitation-emission maps, it is apparent that some oligonucleotides, specifically (ATTT)₃, (ATTT)₇ and (TAT)₄ better suspend SWCNTs of certain chiralities, when comparing to other ssDNAs.

1.4.2. Screening

We have screened the library of 9 ssDNA-SWCNT suspensions with the panel of analytes of interest, which includes D-2-hydroxyglutarate (D2HG), and other structurally-related or contextually-related molecules, such as intermediates in the glycolysis and the TCA cycle, and some of their derivatives (**Scheme 1.1**). These analytes include: glucose, glucose 6-phosphate, fructose 1,6-bisphosphate, pyruvate, citrate, *cis*-aconitate, α-ketoglutarate, succinate, fumarate, malate, oxaloacetate, methylmalonate, glutamate and γ-aminobutyric

19

acid (GABA). SWCNTs of multiple chiralities, in combination with the variety of ssDNA sequences, yield a large pool of potential sensors for molecular recognition accompanied by an optical readout. The results are summarized in a heatmap (**Figure 1.6a**) showing the joint normalized fluorescence response of the (9,5) and (8,7) chiralities peak (around 1284 nm emission wavelength, **Figure 1.6b**) to 10 mM of the respective analyte under 730 nm laser excitation. The (9,5) and (8,7) joint peak was chosen as the basis of comparison, as it showed the largest emission differences, among all other areas of the spectra.

The screening revealed a prominent and unique response of (ATTT)$_7$-SWCNT to D2HG, compared to the fluorescence responses of other ssDNA-SWCNT to D2HG (**Figure 1.6 a** and **c**) and the fluorescence responses of (ATTT)$_7$-SWCNT to other screened analytes (**Figure 1.6 a** and **d**). The interaction of 1 mg L^{-1} of (ATTT)$_7$-SWCNT with 10 mM of D2HG resulted in a 28.2% increase in the SWCNTs fluorescence intensity of the 1285 nm emission peak (**Figure 1.6 a-c, f**), while the response to the structurally similar α-ketoglutarate was statistically insignificant (P = .17).

In order to examine the dependence of the fluorescence response on the excitation and emission wavelengths, we recorded the excitation-emission profile of the (ATTT)$_7$-SWCNT with and without 10 mM D2HG over a range of excitation wavelengths (500-840 nm, every 2 nm, **Figure 1.6d**). Remarkably, the fluorescence response showed a significant excitation wavelength-dependence. Specifically, the 991 nm emission peak, attributed to the (6,5)-SWCNTs, exhibited the largest fluorescence intensity increase of 40.7% under an excitation wavelength of 572 nm, compared to other excitation and emission wavelengths (**Figure 1.6e**). Moreover, the (6,5)-SWCNT, under 572 nm excitation, showed a much smaller response to α-ketoglutarate, whose structure is very similar to D2HG, rendering the (6,5)-SWCNT favorable for distinction between the two compared to the (9,5)+(8,7)-SWCNT responses (**Figure 1.6 c** and **g**).

1.4.3. Sensor allows distinction between optical isomers

The (ATTT)$_7$-SWCNT sensor was challenged with distinguishing between the optical isomers, *D*-2-hydroxyglutarate and *L*-2-hydroxyglutarate (L2HG), which differ by a single bond angle.

We tested the response of (ATTT)$_7$-SWCNT to the analyte panel, now including L2HG, under 572 nm excitation, and found better selectivity, and a significant difference between the fluorescence responses to the two isomers **(Figure 1.6g)**. Compared to 40.7% fluorescence intensity increase in response to D2HG, L2HG induced only 4.5% increase, which is
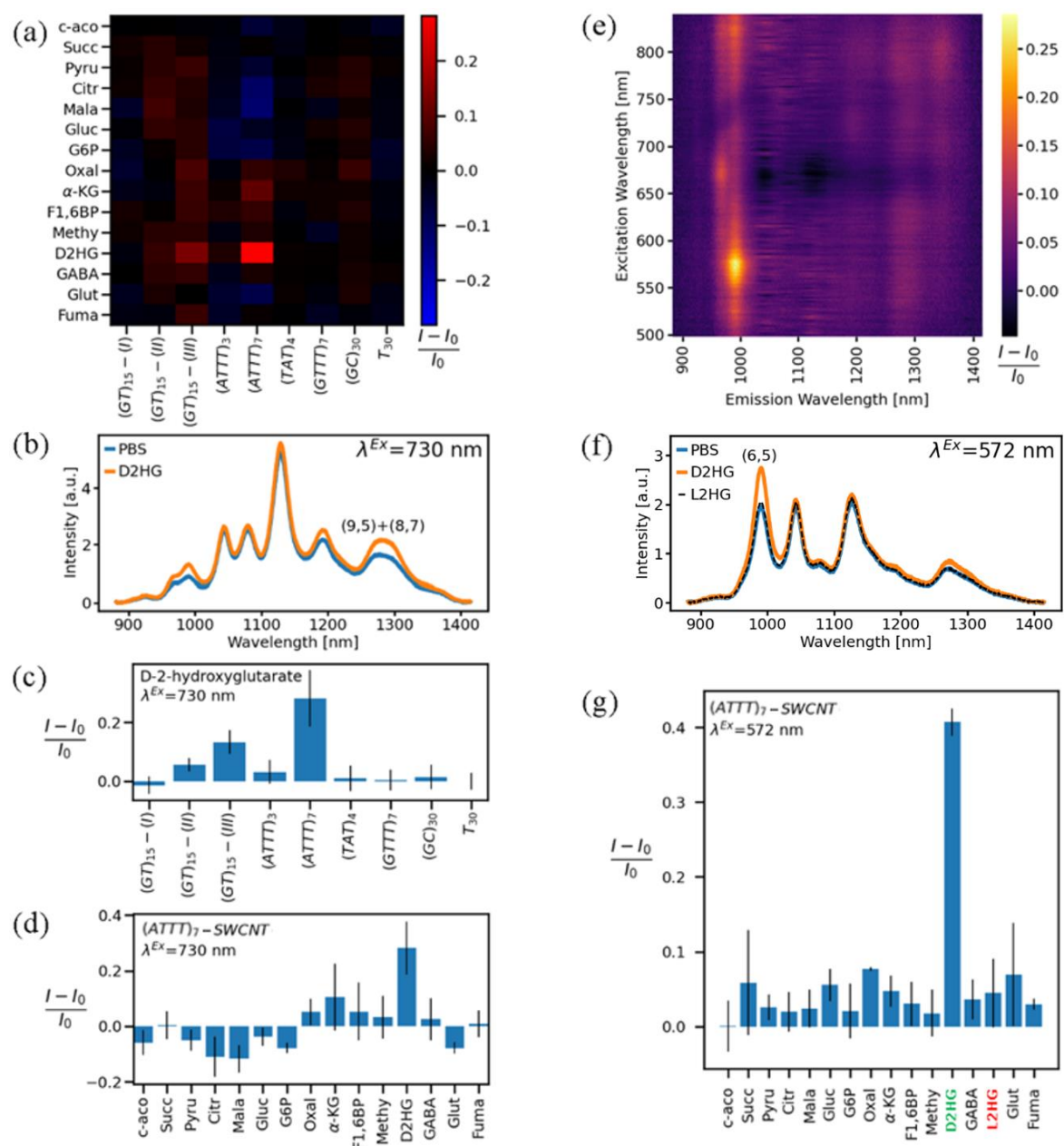

Figure 1.6. Screening results. (a) Normalized fluorescence response heatmap. The horizontal axis represents the various ssDNA-SWCNTs (1 mg·L^{-1}), whereas the vertical axis represents the variety of analytes tested (10 mM). The colormap corresponds to the difference in the fluorescence intensity normalized by the initial fluorescence, in response to the analyte. (b) Fluorescence spectra of (ATTT)$_7$-SWCNT in the nIR, in the presence of D2HG or PBS as control, at excitation wavelength of 730 nm. (c) The normalized difference in fluorescence intensity of all ssDNA-SWCNT combinations in response to D2HG. (d) The normalized difference in fluorescence intensity of (ATTT)$_7$-SWCNT to the tested analytes. (e) Excitation-emission map of the response of (ATTT)$_7$-SWCNT to D2HG. (f) Fluorescence spectra of (ATTT)$_7$-SWCNT in the nIR, in the presence of D2HG, L2HG or PBS as control, at excitation wavelength of 572 nm. (g) Fluorescence responses of (ATTT)$_7$-SWCNT to the screened analytes, including L2HG, the optical isomer of D2HG, under 572 nm laser excitation.

statistically insignificant ($P = .11$). It was previously shown that certain ssDNA-SWCNT combinations exhibit chirality-dependent responses upon molecular recognition[64,66–69]. Moreover, several DNA sequences were shown to preferentially bind one handedness[64], which can in turn affect the fluorescence response to one enantiomer over the other. In our study, some SWCNT chiralities [(9,5), (8,7), (6,5)] were more responsive than others when suspended with (ATTT)$_7$, hinting a possible chirality dependence of the sensor, which might contribute to the obvious distinction between the enantiomers D2HG and L2HG.

1.4.4. (ATTT)$_7$-SWCNT forms a complex and unique conformation

The unique response of (ATTT)$_7$-SWCNT to D2HG cannot be attributed with to chemical features such as the total number of carbon atoms, number of skeletal carbon atoms or number of carboxyl/hydroxyl groups, as well as net charge, molar weight, hydrophobicity (in terms of the predicted partition coefficient logP, calculated by the XLogP3 method[73]), polar surface area, and the number of hydrogen-bond donors or acceptors (**Figure 1.7**). Ruling out these possibilities emphasizes the complexity of the interactions between the sensor and the analyte, and the importance of the unique conformation adopted by the SWCNT corona phase when the DNA adsorbs onto the nanotube scaffold[44,53,74].
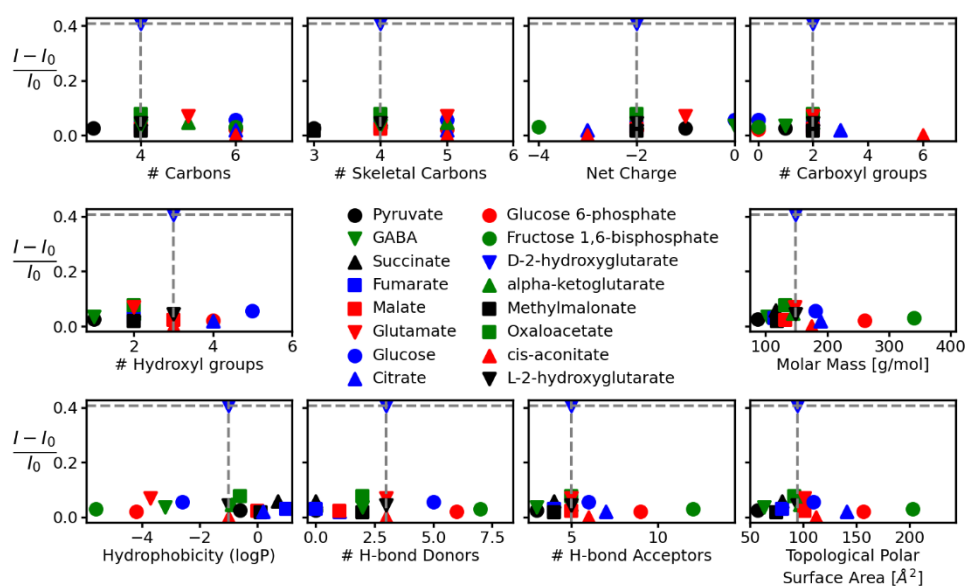
Figure 1.7. Response vs. chemical features. The normalized fluorescence response of (ATTT)$_7$-(6,5)-SWCNT under laser excitation of 572 nm plotted against the chemical features of the tested analytes. The fluorescence response to D2HG is marked by a dashed grey line.

22

1.4.5. The sensor's response is D2HG concentration-dependent

The fluorescence emission of the (ATTT)$_7$-SWCNT sensor for D2HG was recorded over a wide range of D2HG concentrations (0.05 – 64 mg mL^{-1} or 0.34 – 432 mM) for 730 nm and 572 nm laser excitation (**Figure 1.8a**). The fluorescence response of the (9,5) and (8,7) joint peak (1284 nm) and the (6,5) peak (991 nm), respectively, as a function of the D2HG concentration was fitted using the Hill isothermal model, as it accounts for simultaneous or cooperative binding [72], and has been successfully used for fitting SWCNT fluorescence response[41,47,51,52]:

$$\frac{I-I_0}{I_0} = \beta \frac{C^n}{K_d^{\,n}+C^n} \tag{1}$$

Where I_0 and I are the initial and final intensities, respectively, β is a proportionality factor and the maximal relative response at saturation, C is the D2HG concentration, n is the Hill coefficient and K_d is the dissociation constant (**Figure 1.8b** and **Table 1.2**).

|	(9,5) and (8,7) joint peak intensity under 730 nm excitation	(6,5) peak intensity under 572 nm excitation
β	0.46	2.65
K_d [mg mL^{-1}]	2.66	16.02
n	0.66	0.78
Limit of detection	0.641 mg mL^{-1} (3.21 mM)	0.051 mg mL^{-1} (0.256 mM)

Table 1.2. Parameters fitting calibration data to the Hill isothermal model, and the limit of detection.

Although the K_d value of D2HG binding to the (ATTT)$_7$-(6,5)-SWCNT is larger than the K_d value of the (ATTT)$_7$-(9,5)+(8,7)-SWCNT, the maximal response at saturation (the β parameter) is larger for (ATTT)$_7$-(6,5)-SWCNT. These differences are expected owing to the complex interaction of the various chiralities with target analytes which depends of the three dimensional conformation of the corona phase formed by the ssDNA adsorbed onto the nanotube surface[67,71,73,74].

The resultant ranges of detection are 3.21 – 432 mM for the (9,5) and (8,7) joint peak and 0.256 – 432 mM for the (6,5) peak. These ranges coincide with pathological levels of D2HG found in many cancers. For example, in glioma cells the levels are 0.15 - 4.44 mg mL^{-1} (1 – 30 mM), compared to 0.03 – 0.06 mg mL^{-1} (0.2 – 0.4 mM) in healthy tissues, and in acute myeloid

leukemia cells $0.38 - 4.81$ mg mL^{-1} ($2.6 - 32.5$ mM) compared to $0.003 - 0.1$ mg mL^{-1} ($0.02 -$ 0.7 mM) in healthy tissues[75]. In addition, in myeloma the pathological cellular levels of
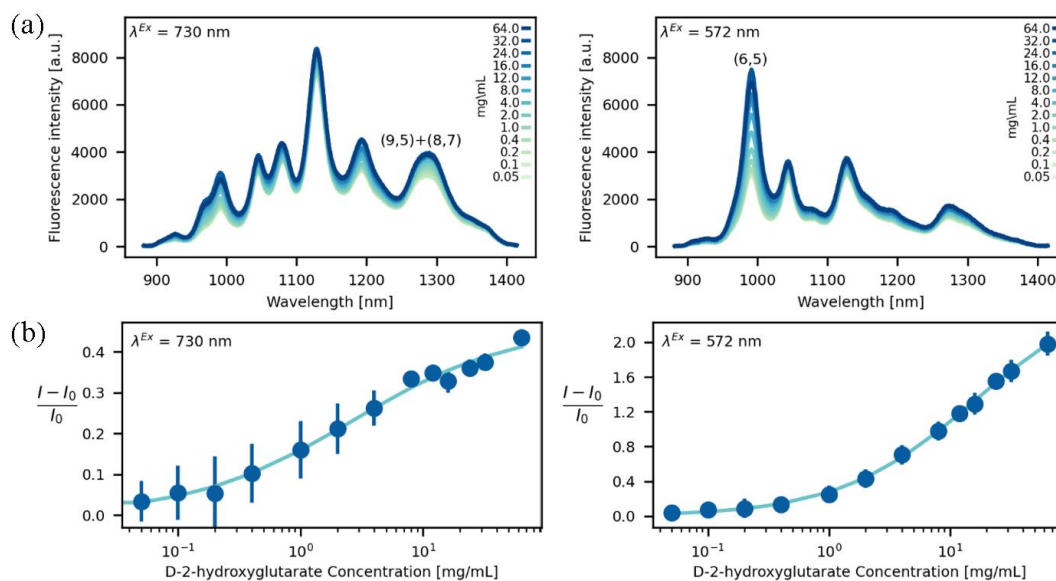
Figure 1.8. Analyte concentration dependence. (a) (ATTT)$_7$-SWCNT nIR fluorescence spectra with increasing concentrations of D2HG, under 730 nm (left) and 572 nm (right) laser excitation. (b) (ATTT)$_7$-SWCNT calibration curve for D2HG, under 730 nm (left) and 572 nm (right) laser excitation. In dark blue – experimental data points, in light blue – Hill model fit.

D2HG, which are associated with the overexpression of the oncogene c-MYC[76], reach 0.15 - 0.59 mg mL^{-1} ($1 - 4$ mM)[75], and in breast cancer, the levels reach $0.07 - 2.96$ mg mL^{-1} ($0.5 - 20$ mM)[75], due to the enzyme alcohol dehydrogenase iron-containing protein 1 (ADHFE1)[75,77] producing D2HG. Hence, our calibration curves can be used to predict the D2HG concentration of an unknown sample, in pathologically relevant levels.

1.5 Conclusion

D-2-hydroxyglutarate is a metabolite which is produced by a mutated TCA cycle enzyme. This mutation is typical of cancers such as gliomas, glioblastomas and leukemia, where the resulting accumulation of D2HG exacerbates mutagenesis and accelerates the cancerous transformation, through multiple potential processes.

We have developed a nanoscale optical sensor for D2HG, based on DNA-functionalized SWCNTs. By comparing fluorescence modulations of the (ATTT)$_7$-SWCNT sensor in the presence of D2HG and its contextual and structural relatives, we found a unique fingerprint of D2HG, which can be used for sensing and quantification of the analyte. Specifically, we characterized the fluorescence response with laser excitation of 572 nm and 730 nm, demonstrating 40.7% and 28.2% fluorescence intensity increase for the 991 nm (6,5)-SWCNTs emission peak and the 1284 nm (9,5)- and (8,7)-SWCNTs joint emission peak, respectively. The high selectivity of the (ATTT)$_7$-(6,5)-SWCNT sensor (under 572 nm laser excitation) towards D2HG, over α-ketoglutarate, holds the possibility of differentiating between mutant and normal isocitrate dehydrogenase activity, thus allowing for indication of a possible cancerous transformation of a cell.

These multi-chirality fluorescence responses allow for more flexibility of light source selection.

Detailed analysis ruled out correlations between the sensor response and a variety of chemical properties of the examined analytes, highlighting the specificity of the recognition. Remarkably, while D2HG resulted in a "turn-on" fluorescence response, its optical isomer, L2HG, did not result in a statistically significant response at all, even though the two share the exact chemical properties excluding a single chiral center. Further, we demonstrated that the normalized fluorescence response of the (ATTT)$_7$-SWCNT sensor can be calibrated against a wide concentration range of D2HG, which can provide a concentration prediction for an unknown sample in levels relevant to many types of cancer cells. The ability of the sensor to report D2HG concentrations, rather than plain presence, can be an important feature for the study of D2HG production and accumulation, and its consequent influence on cellular

functions. For the functioning of the sensor in a more complex environment, such as a cellular environment, a recalibration process might be needed, as adjustments such as these have been demonstrated previously by our group[52].

Our SWCNT nanosensor platform for the D2HG oncometabolite could be used to report on oncometabolite production with subcellular spatial information and high temporal resolution[48,78–80], and thus has the potential to advance basic cancer research.

2. Development of a custom‑made spectrometry data acquisition software

2.1 Introduction

As a large part of our research group is utilizing the near-IR fluorescence of single-walled carbon nanotubes (SWCNTs) for creating sensors, we use a custom-designed devoted spectrometry setup. The setup includes an inverted microscope with a motorized stage, a cryogenically-cooled near-IR detector and laser devices (**Scheme 2.1**).

As experiments usually involve up to several tens of samples, a 96-well plate is our standard container of use. On a typical spectrometry experiment, for a single well, the stage should be adjusted so that light paths of the microscope pass through the center of the well, then excitation light source should be adjusted and applied, and finally, after being diffracted by a grating device, light beams are collected and measured by the detector. As the whole process is repetitive and can take a substantial amount and time and effort, a need for automizing it arises. For this purpose, a fully graphical, user-friendly software was developed, which orchestrates over all participating devices, for making spectra acquisitions from multiple samples easy and effortless.
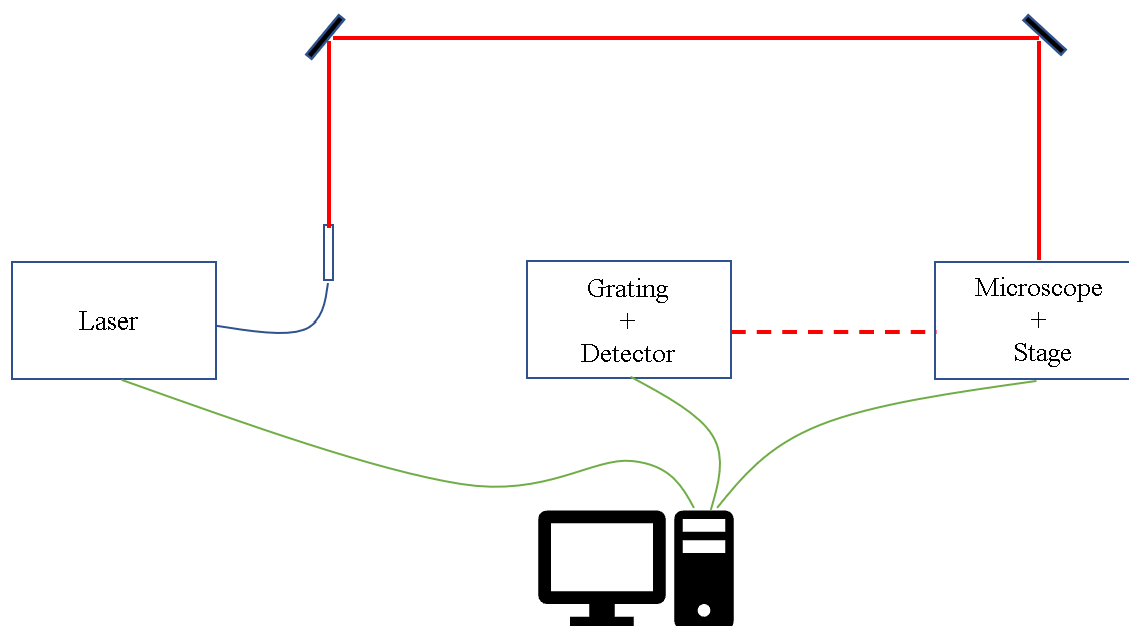
Scheme 2.1 The spectrometry setup. Solid red lines represent laser excitation light, dashed red lines represent light emitted from a sample (fluorescence) and green lines represent computer connections.

2.2 Methods

Programming. The software main presentation layer (frontend, Figure 2.1) was made using the *Kivy* framework and was written in Python 3 and Kivy's KV language. The software backend was written purely in Python 3. The project consists of more than 4700 lines of code divided into 11 files.

Communication with devices is held through dedicated software development kits (SDKs). Specifically, NKT Photonics SDK, Märzhäuser Wetzlar Tango-DLL, and Princeton Instruments PICAM SDK (through C compatibility modules). All hardware functionalities are centered into a standalone *Hardware* class, which can also be used regardless of the UI.

Multithreading. All major hardware interactions are executed in parallel to the main process using python's *threading* module, to avoid process blocking and allow the main event loop to run uninterrupted. Data returned by a device are saved locally within its thread, waiting for collection by the main event loop listener.

Graphics were designed using *Adobe XD* (Figure 2.1)
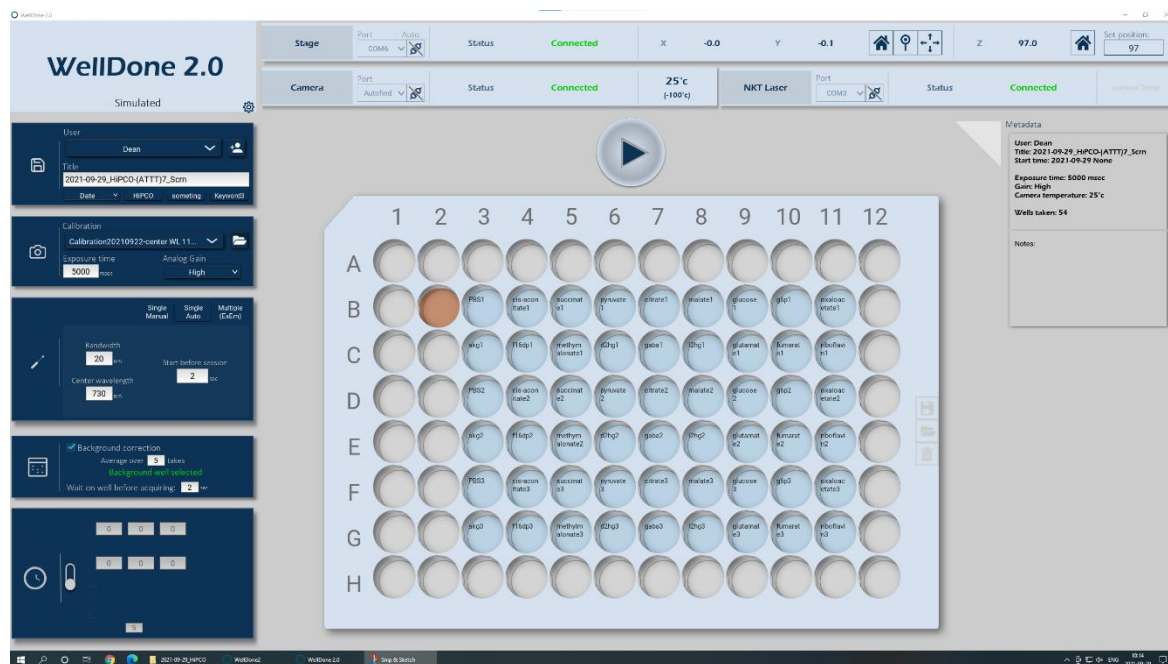
Figure 2.1. The software in plate scanning mode, on a one-time, single excitation wavelength acquisition.

2.3 Results

Hardware interactions. The software is capable of adjusting the detector's exposure time and analog gain, acquiring spectra, and reading its core temperature. It is also capable of adjusting and reading the stage position in 3 axes (xyz), and adjusting the laser's center wavelength and bandwidth, in addition to starting/stopping the laser emission. All hardware interactions were designed to be non-blocking, so the UI is always responsive.

Basic spectra acquisition functionalities include single acquisition of spectra from each of the selected wells, under laser excitation of a single center wavelength (**Figure 2.1**).

Excitation-emission experiments include acquisition of spectra from all selected wells, under laser excitation of a series of predetermined wavelengths (**Figure 2.2a**), which can be a range of wavelength (with a step size of choice), or any custom selection of wavelengths.

Time series acquisition include acquisition of spectra from all selected wells in predetermined time points. It is possible to select a spot to wait on between time points, in order to avoid the laser overheating samples unnecessarily. Moreover, the laser can be shut down automatically between time points, when unneeded (**Figure 2.2b**).

Automatic background correction can be performed, given a well containing the background solution. The method automatically averages multiple reads taken from the background well.

Convenience features. Each selected well for acquisition can be added a title, which will represent its data in the output matrix; Plate layout, together with the added titles, can be saved into a file and loaded for future use; All acquired spectra are displayed in real-time and are easy to navigate (**Figure 2.3**); Metadata is saved with each session.
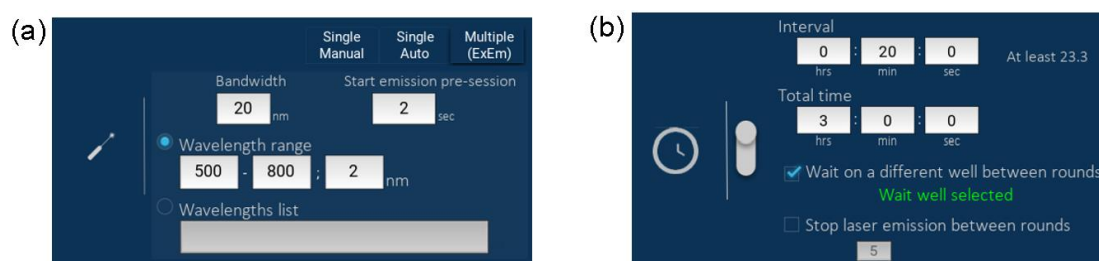
Figure 2.2. Spectra acquisition programs. (a) Options for an excitation-emission experiment. (b) Options for a time series acquisition.
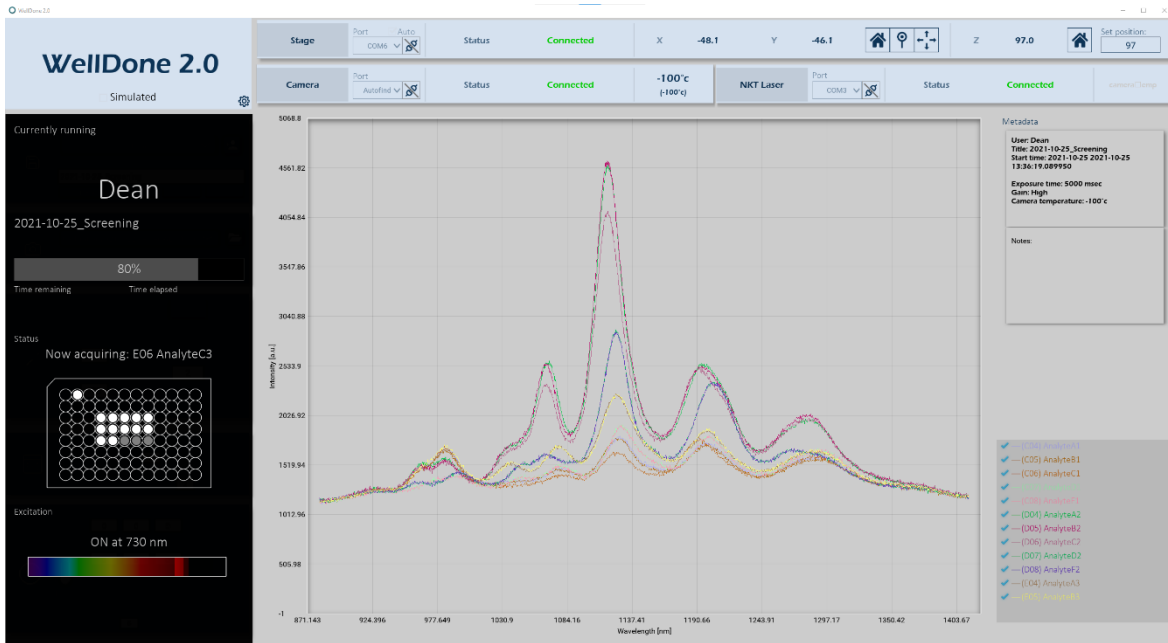
Figure 2.3. Displaying session progress and acquired spectra in real-time.

Live spectra acquisition can be perfomed for the purpose of pre-examining acquisition parameters (detector's exposure time, etc.).

Program outputs include data files (raw and background-corrected, if requested. **Figure 2.4**), metadata PDF file and a session log.

Figure 2.4. Raw spectral data acquired by the software (displayed with Microsoft Excel). Each column in the matrix represents one well.

2.4 Conclusion

A spectrometry data acquisition software was developed, integrating a microscope with a

motorized stage, a laser device and a near-infrared camera. The software automates both

laser excitation and spectra acquisition from 96-well plates, and is easily adjusted in a

designed-to-be-intuitive graphical user interface.

3. References

1. Sciacovelli, M. & Frezza, C. Oncometabolites: Unconventional triggers of oncogenic signalling cascades. *Free Radic. Biol. Med.* **100**, 175–181 (2016).

2. Yang, M., Soga, T. & Pollard, P. J. Oncometabolites: linking altered metabolism with cancer. *3652 J. Clin. Investig.* **123**, (2013).

3. Yang, M., Soga, T., Pollard, P. J. & Adam, J. The emerging role of fumarate as an oncometabolite. *Front. Oncol.* **2**, (2012).

4. Dang, L. *et al.* Cancer-associated IDH1 mutations produce 2-hydroxyglutarate. *Nature* **462**, 739–744 (2009).

5. Chowdhury, R. *et al.* The oncometabolite 2-hydroxyglutarate inhibits histone lysine demethylases. *EMBO Rep.* **12**, 463–469 (2011).

6. Losman, J.-A. *et al.* (R)-2-Hydroxyglutarate is sufficient to promote leukemogenesis and its effects are reversible. *Science (80-.).* **339**, 1621–1625 (2013).

7. Xu, W. *et al.* Oncometabolite 2-hydroxyglutarate is a competitive inhibitor of α-ketoglutarate-dependent dioxygenases. *Cancer Cell* **19**, 17–30 (2011).

8. Böttcher, M. *et al.* D-2-hydroxyglutarate interferes with HIF-1 α stability skewing T-cell metabolism towards oxidative phosphorylation and impairing Th17 polarization. *Oncoimmunology* **7**, 1–12 (2018).

9. Luo, Y., Ma, J. & Lu, W. The significance of mitochondrial dysfunction in cancer. *Int. J. Mol. Sci.* **21**, (2020).

10. Nyhan, W. L. *et al.* D-2-Hydroxyglutaric Aciduria. 137–142

11. Wang, Y. P. & Lei, Q. Y. Metabolic recoding of epigenetics in cancer. *Cancer Commun. (London, England)* **38**, 25 (2018).

12. Pan, J., Li, F. & Choi, J. H. Single-walled carbon nanotubes as optical probes for bio-sensing and imaging. *J. Mater. Chem. B* **5**, 6511–6522 (2017).

13. Alvarez, M. M. *et al.* Emerging trends in micro- and nanoscale technologies in medicine: From basic discoveries to translation. *ACS Nano* **11**, 5195–5214 (2017).

14. Mu, B. *et al.* Recent advances in molecular recognition based on nanoengineered platforms. *Acc. Chem. Res.* **47**, 979–988 (2014).

15. Oh, S.-H. *et al.* Nanophotonic biosensors harnessing van der Waals materials. *Nat. Commun.* **12**, 1–18 (2021).

16. Antonucci, A., Kupis-Rozmysłowicz, J. & Boghossian, A. A. Noncovalent protein

and peptide functionalization of single-walled carbon nanotubes for biodelivery and optical sensing applications. *ACS Appl. Mater. Interfaces* **9**, 11321–11331 (2017).

17. Jorio, A. (Ado), Dresselhaus, G. & Dresselhaus, M. S. Carbon nanotubes: Advanced topics in the synthesis, structure, properties and applications. *Mater. Today* **11**, 57 (2008).

18. Saito, R., Dresselhaus, G. & Dresselhaus, M. S. *Physical Properties of Carbon Nanotubes*. (Published by Imperial College Press and Distributed by World Scientific Publishing Co., 1998). doi:10.1142/p080

19. Zheng, M. Sorting carbon nanotubes. in *Single-Walled Carbon Nanotubes. Topics in Current Chemistry Collections.* 129–164 (Springer, Cham, 2019). doi:10.1007/978-3-030-12700-8_5

20. Bachilo, S. M. *et al.* Structure-assigned optical spectra of single-walled carbon nanotubes. *Science* **298**, 2361–6 (2002).

21. Kruss, S. *et al.* Carbon nanotubes as optical biomedical sensors. *Advanced Drug Delivery Reviews* **65**, 1933–1950 (2013).

22. Jain, A., Homayoun, A., Bannister, C. W. & Yum, K. Single-walled carbon nanotubes as near-infrared optical biosensors for life sciences and biomedicine. *Biotechnol. J.* **10**, 447–459 (2015).

23. Iverson, N. M. *et al.* Quantitative tissue spectroscopy of near infrared fluorescent nanosensor implants. *J. Biomed. Nanotechnol.* **12**, 1035–1047 (2016).

24. Lee, M. A., Bakh, N., Bisker, G., Brown, E. N. & Strano, M. S. A pharmacokinetic model of a tissue implantable cortisol sensor. *Adv. Healthc. Mater.* (2016). doi:10.1002/adhm.201600650

25. Wu, H. *et al.* Monitoring plant health with near-infrared fluorescent H2O2 nanosensors. *Nano Lett.* (2020). doi:10.1021/acs.nanolett.9b05159

26. Lee, M. A. *et al.* Implantable nanosensors for human steroid hormone sensing in vivo using a self-templating corona phase molecular recognition. *Adv. Healthc. Mater.* **9**, 2000429 (2020).

27. Hofferber, E. M. *et al.* Implantable nanotube sensor platform for rapid analyte detection. *Macromol. Biosci.* **19**, 1–8 (2019).

28. Iverson, N. M. *et al.* In vivo biosensing via tissue-localizable near-infrared-fluorescent single-walled carbon nanotubes. *Nat. Nanotechnol.* **8**, 873–880 (2013).

29. Harvey, J. D. *et al.* An in vivo nanosensor measures compartmental doxorubicin exposure. *Nano Lett.* **19**, 4343–4354 (2019).

30.   Bonis-O'Donnell, J. T. D. Del *et al.* Dual near-infrared two-photon microscopy for deep-tissue dopamine nanosensor imaging. *Adv. Funct. Mater.* **27**, 1702112 (2017).

31.   Paviolo, C. & Cognet, L. Near-infrared nanoscopy with carbon-based nanoparticles for the exploration of the brain extracellular space. *Neurobiol. Dis.* **153**, 105328 (2021).

32.   Godin, A. G. *et al.* Single-nanotube tracking reveals the nanoscale organization of the extracellular space in the live brain. *Nat. Nanotechnol.* **12**, 238–243 (2017).

33.   Hong, G. *et al.* Through-skull fluorescence imaging of the brain in a new near-infrared window. *Nat. Photonics* **8**, 723–730 (2014).

34.   Bisker, G., Iverson, N. M., Ahn, J. & Strano, M. S. A pharmacokinetic model of a tissue implantable insulin sensor. *Adv. Healthc. Mater.* **4**, 87–97 (2014).

35.   Moore, V. C. *et al.* Individually Suspended single-walled carbon nanotubes in various surfactants. *Nano Lett.* **3**, 1379–1382 (2003).

36.   Zheng, M. *et al.* DNA-assisted dispersion and separation of carbon nanotubes. *Nat. Mater.* **2**, 338–342 (2003).

37.   Landry, M. P. *et al.* Comparative dynamics and sequence dependence of DNA and RNA binding to single walled carbon nanotubes. *J. Phys. Chem. C* **119**, 10048–10058 (2015).

38.   Farrera, C. *et al.* Carbon nanotubes as optical sensors in biomedicine. *ACS Nano* **11**, 10637–10643 (2017).

39.   Boghossian, A. A. *et al.* Near-infrared fluorescent sensors based on single-walled carbon nanotubes for life sciences applications. *ChemSusChem* (2011). doi:10.1002/cssc.201100070

40.   Hofferber, E. M., Stapleton, J. A. & Iverson, N. M. Review—Single walled carbon nanotubes as optical sensors for biological applications. *J. Electrochem. Soc.* **167**, 037530 (2020).

41.   Zhang, J. *et al.* Molecular recognition using corona phase complexes made of synthetic polymers adsorbed on carbon nanotubes. *Nat. Nanotechnol.* **8**, 959–968 (2013).

42.   Meier, J. *et al.* Quantification of nitric oxide concentration using single-walled carbon nanotube sensors. *Nanomaterials* **11**, 243 (2021).

43.   Card, M., Gravely, M., M. Madani, S. Z. & Roxbury, D. A spin-coated hydrogel platform enables accurate investigation of immobilized individual single-walled carbon nanotubes. *ACS Appl. Mater. Interfaces* acsami.1c06562 (2021).

doi:10.1021/acsami.1c06562

44. Shumeiko, V., Paltiel, Y., Bisker, G., Hayouka, Z. & Shoseyov, O. A nanoscale paper-based near-infrared optical nose (NIRON). *Biosens. Bioelectron.* 112763 (2020). doi:10.1016/j.bios.2020.112763

45. Shumeiko, V. *et al.* A nanoscale optical biosensor based on peptide encapsulated SWCNTs for detection of acetic acid in the gaseous phase. *Sensors Actuators B Chem.* **327**, 128832 (2021).

46. Harvey, J. D. *et al.* A carbon nanotube reporter of microRNA hybridization events in vivo. *Nat. Biomed. Eng.* **1**, 0041 (2017).

47. Kruss, S. *et al.* Neurotransmitter detection using corona phase molecular recognition on fluorescent single-walled carbon nanotube sensors. *J. Am. Chem. Soc.* **136**, 713–724 (2014).

48. Dinarvand, M., Elizarova, S., Daniel, J. & Kruss, S. Imaging of monoamine neurotransmitters with fluorescent nanoscale sensors. *Chempluschem* **85**, 1465–1480 (2020).

49. Beyene, A. G. *et al.* Imaging striatal dopamine release using a nongenetically encoded near infrared fluorescent catecholamine nanosensor. *Sci. Adv.* **5**, eaaw3108 (2019).

50. Bisker, G. *et al.* Protein-targeted corona phase molecular recognition. *Nat. Commun.* **7**, 1–14 (2016).

51. Bisker, G. *et al.* Insulin detection using a corona phase molecular recognition site on single-walled carbon nanotubes. *ACS Sensors* **8**, 367–377 (2018).

52. Ehrlich, R., Hendler-Neumark, A., Wulf, V., Amir, D. & Bisker, G. Optical nanosensors for real-time feedback on insulin secretion by β-cells. *Small* 2101660 (2021). doi:10.1002/smll.202101660

53. Pinals, R. L. *et al.* Rapid SARS-CoV-2 spike protein detection by carbon nanotube-based near-infrared nanosensors. *Nano Lett.* **21**, 2272–2280 (2021).

54. Williams, R. M., Harvey, J. D., Budhathoki-Uprety, J. & Heller, D. A. Glutathione-S-transferase fusion protein nanosensor. *Nano Lett.* **20**, 7287–7295 (2020).

55. Hendler-Neumark, A. & Bisker, G. Fluorescent single-walled carbon nanotubes for protein detection. *Sensors (Switzerland)* **19**, (2019).

56. Yaari, Z. *et al.* Nanoreporter of an enzymatic suicide inactivation pathway. *Nano Lett.* **20**, 7819–7827 (2020).

57. Shumeiko, V., Paltiel, Y., Bisker, G., Hayouka, Z. & Shoseyov, O. A Paper-based

near-infrared optical biosensor for quantitative detection of protease activity using peptide-encapsulated SWCNTs. *Sensors* **20**, 5247 (2020).

58.   Wulf, V., Slor, G., Rathee, P., Amir, R. & Bisker, G. Dendron-polymer hybrids as tailorable coronae of single-walled carbon nanotube. *ChemRxiv* 10.26434/chemrxiv.14452785.v1 (2021). doi:10.26434/chemrxiv.14452785.v1

59.   Warner, J. B. & Lolkema, J. S. Growth of Bacillus subtilis on citrate and isocitrate is supported by the Mg2+−citrate transporter CitM. *Microbiology* **148**, 3405–3412 (2002).

60.   Kim, S. *et al.* PubChem in 2021: New data content and improved web interfaces. *Nucleic Acids Res.* **49**, D1388–D1395 (2021).

61.   Shankar, A., Mittal, J. & Jagota, A. Binding between DNA and Carbon Nanotubes Strongly Depends upon Sequence and Chirality. *Langmuir* **30**, 3176–3183 (2014).

62.   Yang, F. *et al.* Chirality Pure Carbon Nanotubes: Growth, sorting, and characterization. *Chemical Reviews* (2020). doi:10.1021/acs.chemrev.9b00835

63.   Yang, Y., Sharma, A., Noetinger, G., Zheng, M. & Jagota, A. Pathway-dependent structures of DNA-wrapped carbon nanotubes: Direct sonication vs surfactant/DNA exchange. *J. Phys. Chem. C* **124**, 9045–9055 (2020).

64.   Ao, G., Streit, J. K., Fagan, J. A. & Zheng, M. Differentiating left- and right-handed carbon nanotubes by DNA. *J. Am. Chem. Soc.* **138**, 16677–16685 (2016).

65.   Zheng, M. Structure-based carbon nanotube sorting by sequence-dependent DNA assembly. *Science (80-.).* **302**, 1545–1548 (2003).

66.   Xu, L. *et al.* Enantiomeric separation of semiconducting single-walled carbon nanotubes by acid cleavable chiral polyfluorene. *ACS Nano* **15**, 4699–4709 (2021).

67.   Salem, D. P. *et al.* Chirality dependent corona phase molecular recognition of DNA-wrapped carbon nanotubes. *Carbon N. Y.* **97**, (2016).

68.   Li, H. *et al.* Separation of specific single-enantiomer single-wall carbon nanotubes in the large-diameter regime. *ACS Nano* **14**, 948–963 (2020).

69.   Castillo, M., Pho, C., Naumov, A. V. & Dzyuba, S. V. Modulating chirality-selective photoluminescence of single-walled carbon nanotubes by ionic liquids. *J. Phys. Chem. Lett.* **9**, 6689–6694 (2018).

70.   Cheng, T. *et al.* Computation of octanol−water partition coefficients by guiding an additive model with knowledge. *J. Chem. Inf. Model.* **47**, 2140–2148 (2007).

71.   Bisker, G. *et al.* A mathematical formulation and solution of the CoPhMoRe inverse problem for helically wrapping polymer corona phases on cylindrical substrates. *J.*

Phys. Chem. C **119**, 13876–13886 (2015).

72. Weiss, J. N. The Hill equation revisited: uses and misuses. *FASEB J.* **11**, 835–841 (1997).

73. Nißler, R. *et al.* Sensing with chirality-pure near-infrared fluorescent carbon nanotubes. *Anal. Chem.* 44–47 (2021). doi:10.1021/acs.analchem.1c00168

74. Tu, X., Manohar, S., Jagota, A. & Zheng, M. DNA sequence motifs for structure-specific recognition and separation of carbon nanotubes. *Nature* **460**, 250–253 (2009).

75. Ježek, P. 2-Hydroxyglutarate in cancer cells. *Antioxid. Redox Signal.* **33**, 903–926 (2020).

76. Gonsalves, W. I. *et al.* Glutamine-derived 2-hydroxyglutarate is associated with disease progression in plasma cell malignancies. *JCI insight* **3**, (2018).

77. Mishra, P. *et al.* ADHFE1 is a breast cancer oncogene and induces metabolic reprogramming. *J. Clin. Invest.* **128**, 323–340 (2018).

78. Gravely, M. & Roxbury, D. Multispectral fingerprinting resolves dynamics of nanomaterial trafficking in primary endothelial cells. *ACS Nano* acsnano.1c04500 (2021). doi:10.1021/acsnano.1c04500

79. Williams, R. M. *et al.* Harnessing nanotechnology to expand the toolbox of chemical biology. *Nature Chemical Biology* **17**, 129–137 (2021).

80. Jena, P. V. *et al.* A carbon nanotube optical reporter maps endolysosomal lipid flux. *ACS Nano* acsnano.7b04743 (2017). doi:10.1021/acsnano.7b04743

תקציר

ייצור של אונקו-מטבוליטים הוא תוצאה ישירה של מוטגנזה באנזימים המשתתפים בתהליכים מטבוליים תאיים, המופיעה בדרך כלל בסרטן מסוג גליומה, גליובלסטומה ולויקמיה. בהצטברם, אונקו-מטבוליטים מקדמים את תהליך ההתמרה הסרטנית, מתוך התערבותם בתהליכים תאיים חשובים. מכאן שהיכולת לאתר ולכמת אונקו-מטבוליטים הינה חיונית למחקר הסרטן ולדיאגנוזה קלינית. בעבודה זו, אנו מציגים ננו-חיישן אופטי בתחום התת-אדום הקרוב (near infrared) לאונקו-מטבוליט ידוע, D-2-hydroxyglutarate (D2HG). החיישן נתגלה בסריקה של ספריית ננו-צינוריות פחמן חד- שכבתיות פלואורוסצנטיות (Single-walled carbon nanotubes – SWCNT), שהורכבו עם DNA חד- גדילי. תהליך הסריקה הנרחב התאפשר הודות לפיתוחה של תוכנה ייעודית לשליטה במיכשור ספקטרומטרי ולרכישת סיגנל ספקטרומטרי באופן אוטומטי.

הסריקה מצאה את הצירוף SWCNT-(ATTT)₇ כחיישן ל-D2HG, שהדגים הגברה בעוצמת הפלואורסנציה בחשיפה לאונקו-מטבוליט. נמצא שלא ניתן לייחס את תגובות הפלואורסנציה של החיישן למאפיינים כימיים בסיסיים של האנליטים שנבחנו, ועל כן הוא בעל יכולת גבוהה להבחין בין D2HG לבין מטבוליטים דומים, ואף נראה כמבחין בין D2HG לבין האיזומר האופטי שלו, L-2-hydroxyglutarate. בנוסף, נמצא כי השינויים בפלואורסנציה תלויים בריכוז האנליט ובכירליות של ה-SWCNT, אשר מדגימים הגברת עוצמה של עד 40.7% ו-28.2% בסיגנל השייך לכירליות (6,5) ובסיגנל המשותף לכירליות (9,5) ו-(8,7), בהתאמה, תחת אקסיטציית לייזר באורכי גל של 572 ננומטר ו-730 ננומטר, בהתאמה, בנוכחות 10 mM של D2HG.

עבודה זו פותחת אפשרויות חדשות לזיהוי מולקולרי של אונקו-מטבוליטים, היכולות לקדם את מחקר מחלת הסרטן והשינויים המטבוליים הטיפוסיים לה.

אוניברסיטת תל אביב

זיהוי אונקו-מטבוליטים באמצעות ננו-צינוריות פחמן חד-שכבתיות פלואורסצנטיות

חיבור זה הוגש כעבודת גמר לקראת תואר "מוסמך אוניברסיטה" בהנדסה ביו-רפואית

על ידי

דין אמיר

המחקר התבצע במחלקה להנדסה ביו-רפואית
תחת הנחייתה של דר' גילי ביסקר

אוקטובר 2021

זיהוי אונקו-מטבוליטים באמצעות ננו-צינוריות פחמן חד-שכבתיות פלואורסצנטיות

חיבור זה הוגש כעבודת גמר לקראת תואר "מוסמך אוניברסיטה" בהנדסה ביו-רפואית

על ידי

דין אמיר

אוקטובר 2021